

Spectroscopic Analysis for the Identification of Loss Mechanisms in Back-Contact Perovskite Solar Cells

Hongyu Sun, Sarah Gillespie, Susan A. Rigter, Julia S. van der Burgt, Kunal Datta, and Erik C. Garnett*

Back-contact perovskite solar cells offer a significant potential to reach high efficiency due to reduced parasitic absorption from the top surface. However, the currently reported efficiencies are considerably lower (<10%) than planar perovskite solar cells (>20%). Herein, back-contact perovskite solar cells are fabricated to study loss mechanisms that cause low device efficiency. This work spatially resolves the short-circuit current, open-circuit voltage, photoluminescence quantum yield, carrier lifetime, and external quantum efficiency of the devices. The results indicate that the front surface recombination, increased nonradiative recombination at hole contact layer/perovskite interface, and the extraction barriers are three main mechanisms limiting devices from achieving high efficiencies.

and the cathode are located at the rear of the photoabsorber layer, rendering the front-facing surface available for antireflection coatings and transparent passivating layers to be deposited.^[1] Furthermore, these layers can be deposited without the constraint of requiring electrical conductivity. The strongest advantage of the BC cell is that parasitic absorption and reflection associated with the top electrode in the planar counterpart are nearly eliminated, while the front surface can be completely passivated. These improvements have been shown to increase the absolute short-circuit current density (J_{sc}) by more than 3.6% in silicon PV.^[5–7]

1. Introduction

The world record cell efficiency in crystalline silicon photovoltaics (PV) currently stands at 26.7%, just $\approx 2.1\%$ lower than the maximum achievable power conversion efficiency (PCE) when realistic losses such as Auger and light trapping are considered.^[1–3] The record performance in silicon PV is mainly attributed to the complete interdigitated back-contact (IBC) heterojunction design.^[1,4] In the back-contact (BC) configuration, both the anode

While IBC Si cells are commercially available, back-contact configurations in emerging, efficient PV such as III–V, CdTe, CIGS, and perovskite devices have been relatively less explored.^[8–19] The key difference between silicon and such emerging technologies is the nature of the absorber layer. For silicon, which has an indirect bandgap, the minority carrier-diffusion length (L_d) is on the order of 100–1000 μm .^[20,21] In comparison, organic–inorganic perovskite materials, which are the primary focus of this paper, demonstrate L_d on the order of 1–10 μm .^[22–25] Consequently, advanced processing such as photolithography is necessary to achieve the required scale and positioning of the back contacts for efficient carrier extraction. There are few reports implementing BC configurations in perovskite solar cells, exploiting various BC architectures such as quasi-interdigitated back-contact, honeycomb like structures, and micron-sized V-shaped grooves.^[14–19] Such works have reported device efficiencies between 3.2% and 10.5%.

An advantage in studying BC structures in novel PV technologies is that the exposed front surface allows us to optically and electrically probe interfaces between the contacts and absorber material. In turn, these spatially resolved scans yield insights into the carrier generation, recombination, and transport mechanisms, thereby enabling us to identify and mitigate remaining loss pathways—for both the BC cell and the corresponding planar configuration.^[39]

Here, we develop a BC solar cell based on our previously proposed theoretical design.^[26] In this architecture, the Ni anode, NiO_x hole transport layer (HTL) and Al_2O_3 dielectric spacer are fabricated in a square grid array with a pitch of 12 μm and linewidth of 4 μm . The grid is fabricated on top of a planar SnO_2 electron transport layer (ETL), with the perovskite layer


H. Sun, S. Gillespie, S. A. Rigter, J. S. van der Burgt, E. C. Garnett
AMOLF Institute

Science Park 104, Amsterdam 1098XG, The Netherlands
E-mail: e.c.garnett@uva.nl

S. Gillespie
TNO Energy Transition
Westerduinweg 3, Petten 1755LE, Netherlands

S. A. Rigter, E. C. Garnett
Institute of Physics
University of Amsterdam
Science Park 904, Amsterdam 1098XH, The Netherlands

K. Datta
Molecular Materials and Nanosystems and Institute for Complex Molecular Systems
Eindhoven University of Technology
5600 MB Eindhoven, Eindhoven The Netherlands

 The ORCID identification number(s) for the author(s) of this article can be found under <https://doi.org/10.1002/admt.202300241>

© 2023 The Authors. Advanced Materials Technologies published by Wiley-VCH GmbH. This is an open access article under the terms of the Creative Commons Attribution License, which permits use, distribution and reproduction in any medium, provided the original work is properly cited.

DOI: 10.1002/admt.202300241

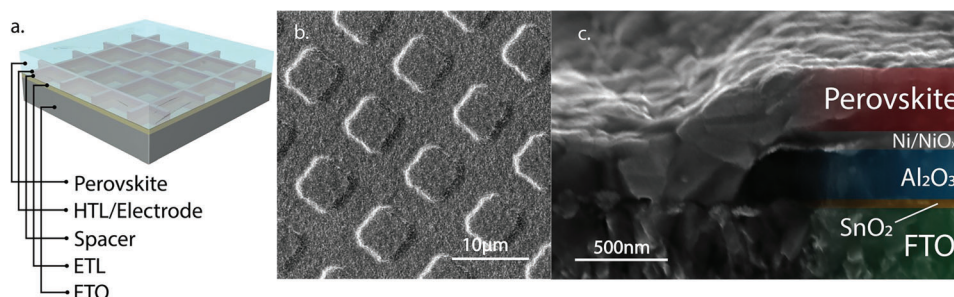


Figure 1. a) Schematic of the back-contact perovskite solar cell configuration considered in this work. A full conformal layer of SnO₂ is deposited on the FTO/glass substrate. The Ni@NiO_x/Al₂O₃ (anode@HTL/spacer) grid is patterned on top of the substrate. A 300 nm Al₂O₃ spacer layer separates the SnO₂ and NiO_x layers. The triple cation perovskite is coated on top of both contacts. b) Top-view scanning electron micrograph (SEM) of the device after perovskite deposition. Shaded areas indicate that the topography of the perovskite layer follows the grid pattern beneath the film. c) SEM cross-section of the device.

deposited on top of both contacts. We report a PCE of 4.83% for a 4 mm² cell, using a triple cation perovskite active layer with a nominal composition of Cs_{0.1}(FA_{0.8}MA_{0.2})_{0.9}Pb(I_{0.8}Br_{0.2})₃. Moreover, we investigate the device performance limitations by spatially resolving the optical and electrical characteristics using a home-built integrating sphere microscopy setup combined with a piezoelectric stage, as described in our previous works.^[27,28] We map the local photogenerated current and open-circuit voltage (V_{OC}), absorption, external quantum yield (EQE), photoluminescence quantum yield (PLQY), and lifetime, across the device surface and use this data to identify loss mechanisms and propose potential points for improvement.

2. Device Structure

The fabricated BC perovskite device considered in this study is schematically depicted in **Figure 1a**. Generally, for IBC cells, photolithographic alignment is required to position the different carrier selective contacts across the device.^[29,30] As only one contact is patterned in our device, photolithographic alignment is not necessary which significantly simplifies the fabrication procedure compared to the conventional IBC cell.

The full fabrication procedure of the device is outlined in detail in Figure S1 in the Supporting Information. Briefly, 60 nm of SnO₂ is grown on a cleaned FTO glass substrate by chemical bath deposition. The chemical bath growth method has been shown to form conformal, pinhole-free coverage of SnO₂, resulting in higher performing devices compared to spin-coated SnO₂ layers.^[31,32] Potassium iodide is spin-coated on the SnO₂ to passivate the surface, followed by an anneal at 100 °C for 10 min in air.^[40]

To fabricate the grid contact, a photoresist adhesion layer (hexamethyldisilazane) and a negative photoresist (Ma-N 1410) are sequentially deposited on the substrate. The grid pattern is developed through a mask by UV lithography. The grid consists of a 12 μm pitch with a linewidth of 4 μm (Figure 1b). Following the development of the pattern in the resist, 500 nm thick grids consisting of 300 nm of an Al₂O₃ spacer and 200 nm of Ni are sequentially deposited on the sample by e-beam evaporation. The thickness of grids is optimized to 500 nm by comparing efficiencies using a sample set with 420, 460, and 500 nm thick grids. The result is summarized in Figure S2 (Support-

ing Information). The sample is kept overnight in *N*-methyl-2-pyrrolidone to lift off the remaining photoresist and the undesired metal. The samples are then UV ozone treated for 45 min to form an oxide seed layer and annealed at 300 °C for 1 h under ambient air. The anneal yields the desired core-shell Ni-NiO_x structure, where the Ni and NiO_x function as the anode and the hole transport layer, respectively.^[19] Finally, a solution of Cs_{0.1}(FA_{0.8}MA_{0.2})_{0.9}Pb(I_{0.8}Br_{0.2})₃ is spin-coated on top of the sample in a N₂ atmosphere and annealed at 100 °C for 1 h.^[33,34] The details of the perovskite film preparation are described in the Supporting Information. The thickness of the perovskite on the SnO₂ surface is measured to be 418 nm by a profilometer (Figure S3, Supporting Information). The cross-sectional SEM in Figure 1c indicates that the perovskite film is not planarized across the surface; rather, it follows the topography of the underlying grid. The top surface of the device is intentionally not capped so that device properties can be analyzed without considering parasitic absorption. However, high efficiency BC solar cells generally employ a passivating layer and antireflective coating on top of the photoabsorber to minimize front surface recombination velocity, increase photoabsorption and enhance the overall efficiency of the device.^[41]

3. Results

3.1. Photovoltaic Cell Performance

The photocurrent density–voltage (J – V) scan was measured at 1 Sun under standard AM1.5G,

1000 W m⁻², 25 °C test conditions. The forward (0 V → V_{OC}) and reverse (V_{OC} → 0 V) J – V sweeps are shown in **Figure 2a**. The V_{OC} = 0.77 V, J_{SC} = 14.4 mA cm⁻², and fill factor (FF) = 0.38 for the forward sweep, and V_{OC} = 0.79 V, J_{SC} = 12.5 mA cm⁻², and FF = 0.49 for the reverse sweep. These parameters correspond to respective device efficiencies of 4.26% and 4.83%. To identify loss pathways resulting in the low PCE in this device, we measured the spatially resolved electrical characteristics using focused laser scanning microscopy, which enables photocurrent and photovoltage generated from the laser scanning to be mapped. More information is provided in the Supporting Information of this paper. Figure 2b depicts the local current generated from a focused 720 nm laser when scanned across a 30 × 30 μm² area of the cell.

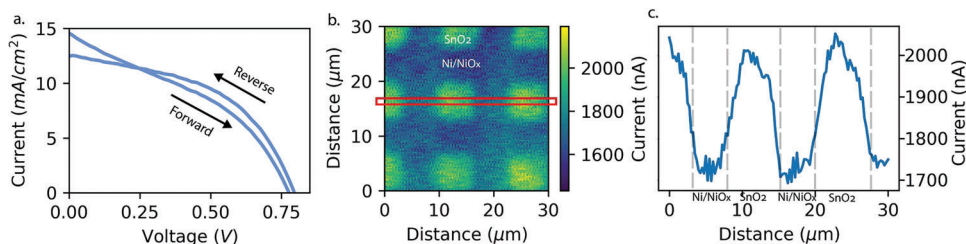


Figure 2. a) Forward and reverse J - V sweeps measured over a 1mm^2 cell area under 1 Sun standard test conditions b) 2D map of locally generated photocurrent 720 nm laser excitation scanned across the device. The color scale (right) indicates the absolute photocurrent generated at the film above the different contacts, with the SnO_2 ETL opening exhibiting higher currents than the Ni@NiO_x HTL/anode grid. c) Average line scan of the generated current measured within the red box highlighted in (b), with the different contact layer regions labeled.

The local current generated on the perovskite located above the Ni@NiO_x grid is $\approx 17.6\%$ (300 nA) lower than the local current generated above the planar SnO_2/FTO substrate. The V_{OC} generated upon laser excitation was also mapped. Similar patterns are observed, as shown in Figure S4 (Supporting Information). Further resolving the photocurrent variation between the contacts, Figure 2c plots the average line scan of the photocurrent highlighted in Figure 2b.

3.2. Optical Scanning Microscopy

To further investigate the mechanisms behind the observed spatial variations in photocurrent and photovoltage over the device, we measured key optical properties of the device, namely the ab-

sorptance, PLQY and PL lifetime. We measure the steady-state optical properties with an integrating sphere microscopy set up, coupled to a supercontinuum laser and a piezoelectric stage.^[27,28]

Figure 3a shows the measured absorbance of the device, scanned with a 650 nm laser over a $24 \times 24 \mu\text{m}^2$ area. On average, 70% of the incident light is absorbed by the perovskite layer located directly above the $\text{SnO}_2/\text{FTO}/\text{glass}$ substrate. The fraction of absorbed light increases to 79% in the region above the Ni@NiO_x grid. As the perovskite layer was measured to be 418 nm thick above the SnO_2 and 411 nm thick above the grid (Figure S2, Supporting Information), the enhanced absorption is not a result of layer thickness. Rather, we attribute the increase to the metallic Ni anode in the grid acting as a back reflector of light. However, despite the higher absorption, we observe the opposite behavior in photocurrent generation (Figure 2b). Given the relatively flat

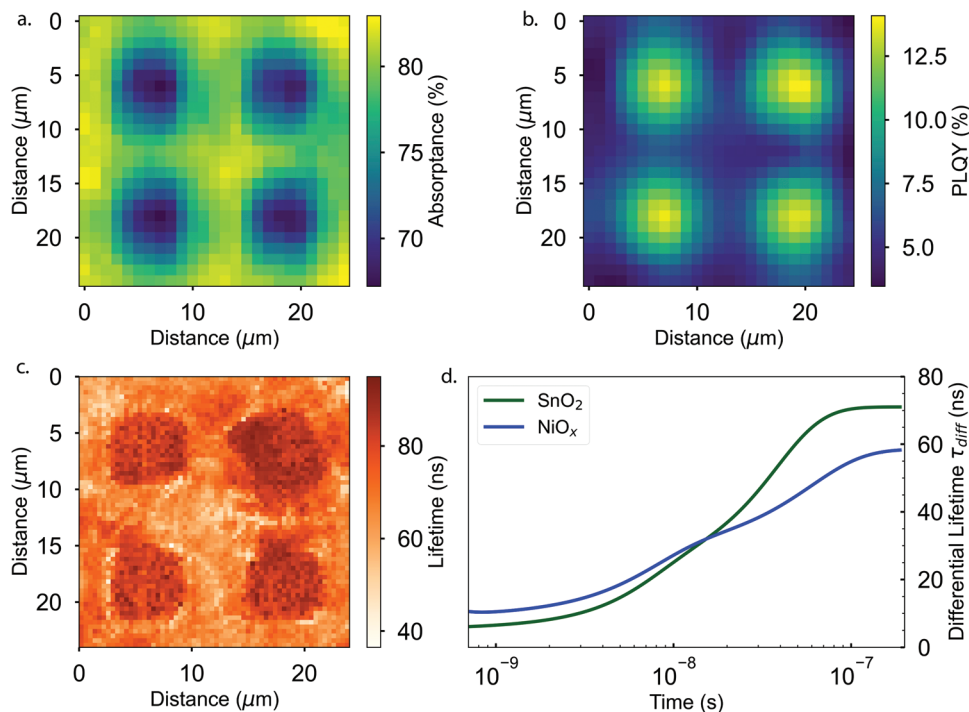


Figure 3. a) Absorbance map across a $24 \mu\text{m} \times 24 \mu\text{m}$ device area. The absorption is enhanced at measured regions of where the perovskite film is located above the Ni@NiO_x grid, compared to regions of above the SnO_2 . b) Spatially resolved PLQY across the same $24 \mu\text{m} \times 24 \mu\text{m}$ device area. c) The average PL lifetime mapped across the area using FLIM with TCSPC. d) The fitting of differential lifetime on the two contact regions (Ni@NiO_x grid and SnO_2) over a larger ($80 \mu\text{m} \times 80 \mu\text{m}$) area that includes the map in panel c (for complete area lifetime map see Figure S5 in the Supporting Information).

photocurrent profile on the NiO_x and that the highest photocurrent is observed in the center of the SnO₂ regions (Figure 2b,c), we discount carrier diffusion as the dominant factor in this spatial modulation (photocurrent would then be expected to peak at the electrode grid edge). Instead, our results point to a higher carrier recombination rate above the Ni@NiO_x grid compared to the SnO₂/FTO contact.

Further examining the optical properties, the PLQY measured across the device under 650nm laser excitation is shown in Figure 3b. The PLQY deviates significantly between the SnO₂/FTO opening and directly above the Ni@NiO_x grid which show the PLQY of 13% and 5% on average, respectively. This is consistent with the higher nonradiative recombination rate above the HTL regions compared to the ETL regions.

From the PLQY- V_{OC} relation: $V_{OC,imp} = V_{OC,rad} + V_{therm} \ln(PLQY)$, where $V_{OC,imp}$ is the implied V_{OC} , V_{therm} is the thermal voltage = 25.7 mV at 25 °C and $V_{OC,rad}$ is the V_{OC} at the radiative limit.^[36–38] The actual V_{OC} from the device assuming perfect carrier extraction should be 1.12V based on the relation shown above. However, considering the measured V_{OC} of 0.79V, a big loss exists in our device which indicates a V_{OC} loss from an extraction barrier at the contact.

To test this hypothesis, we conduct spatially resolved PL lifetime measurements under a 485 nm pulsed laser excitation using time correlated single photon counting microscopy (TCSPC). The average PL lifetime—calculated at each pixel using fluorescence lifetime imaging microscopy (FLIM)—is mapped in Figure 3c^[35]. The complete 80 μm × 80 μm scan and the separated complete average lifetime histograms are included in Figure S5 (Supporting Information). The calculations deriving the average PL lifetime are included in the Supporting Information Section 6. The transient PL decay curves for each of the separated NiO_x and SnO₂ contact regions are plotted in Figure S5b (Supporting Information). A high order fitting procedure was applied to these curves and the differential lifetime

$$T_{diff} = -\left(\frac{1}{2} \frac{d \ln(\Phi_{PL})}{dt}\right)^{-1} \quad (1)$$

is calculated at every time point for the separated contact regions and is shown in Figure 3d^[42]. From the definition of the differential lifetime, the plateaus of each of the two curves at low carrier density (that is, at longer times, i.e., after 10⁻⁷ s) are the effective nonradiative recombination lifetimes. This was found to be $T_{NiO_x} = 58$ ns for $T_{SnO_2} = 71$ ns. Extended details on the differential lifetime definition and decay curve fitting procedure, in addition to the differences in the differential lifetime and the average PL lifetime are provided in the Supporting Information.

The 22% longer lifetime on SnO₂ suggests a higher rate of nonradiative recombination on the HTL as compared to the ETL. Assuming that the bulk nonradiative lifetime of the perovskite is the same across both contact regions, it is therefore likely that this difference arises from higher interfacial carrier recombination at the NiO_x interface, compared to the SnO₂ interface.

3.3. EQE Line Scan

Figure 4 shows EQE measurement results for SnO₂ and Ni@NiO_x device regions. The EQE was obtained by measuring the photocurrent of the device and varying the incident laser wavelength across the visible range ($\lambda = 480$ –780 nm). As part of the measurement, white bias light is mixed with the chopped laser to help the device reach the injection level expected under solar illumination. The details of the measurement are described in Section 4 of the Supporting Information. Considering the energy barriers of the contacts, there is a marked decrease in absolute EQE over all wavelengths when the laser is scanned over the HTL grid (Figure 4b). At $\lambda_{ex} = 700$ nm, there is a 17% drop in EQE over the HTL grid compared to the ETL substrate (Figure 4c). Notably, we observed a trend of decreasing EQE from longer wavelength 700 nm to shorter wavelength 480 nm. Additionally, the difference between EQE on two contacts becomes smaller toward shorter wavelengths. A current scanning map at 410 nm is performed as a supplement to this observation (Figure S4, Supporting Information). The map shows a lower current value than at 710 nm and spatially uniform photocurrent and photovoltage maps.

$$J_{SC} = -q \int_{\lambda_1}^{\lambda_2} EQE(\lambda) \Phi(\lambda) d\lambda \quad (2)$$

The measured EQE can be integrated over wavelength to calculate the expected short-circuit current density by the standard relation (Equation (1)), where Φ is the spectral photon flux.^[36] By integrating the EQE, we obtain the J_{SC} value of 10.17 mA cm⁻² which is about 20% lower than the J_{SC} extracted from the J - V curve (Figure 2). This difference is partially explained by the smaller range over which we can measure the EQE (only to 480 nm due to laser bandwidth restrictions) and partially from the difficulty in satisfying the condition of the chopped laser being a small perturbation on the light bias while also having sufficient signal. Nevertheless, the general trend of lower EQE at shorter wavelengths was present for different light bias values (see Figure S6 in the Supporting Information).

4. Discussion

Combining the results shown above, the loss mechanisms of back-contact perovskite solar cells can be described as the follows. First, we see that the front surface recombination plays a significant role. Due to the lack of a top contact, carriers generated in the perovskite film have to diffuse through the entire layer to reach the back contacts. For shorter wavelengths, the carriers are generated close to the top surface where surface recombination dominates the loss because of the unpassivated top surface. For longer wavelengths, the carriers are generated closer to the back contacts on average, which minimizes the need for vertical diffusion. This hypothesis is supported by the EQE, which shows an increasing EQE value from shorter wavelengths to longer wavelengths everywhere on the device (Figure 4a,b).

Increased nonradiative recombination rates at the HTL/perovskite interface compared to the ETL/perovskite provides a second major loss mechanism. This is supported

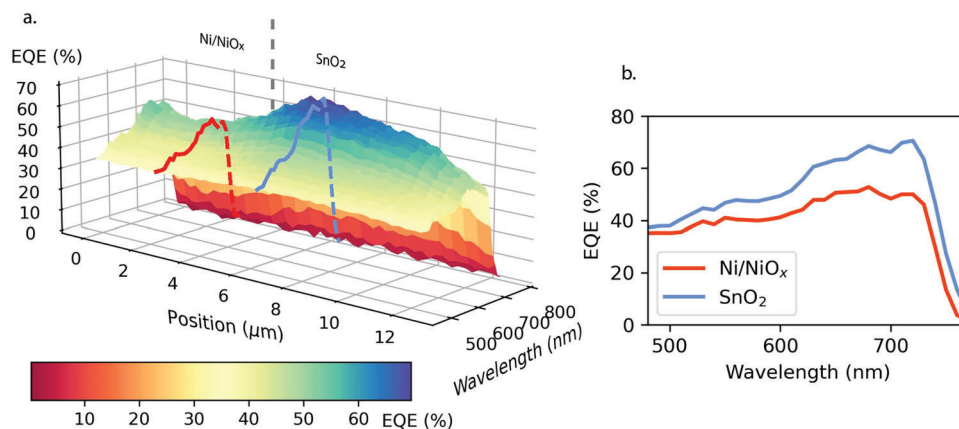


Figure 4. a) The external quantum efficiency obtained from a spectral sweep of $\lambda_{\text{ex}} = 480\text{--}780\text{ nm}$. b) Single EQE scans measured across the SnO_2 ETL region (blue) and Ni@NiO_x (red). These scans are labeled in (a).

by the lower PLQY and PL lifetime as well as lower EQE over the HTL regions (Figures 3b–d and 4a,b). The ETL regions have lower nonradiative recombination rates than both the air/perovskite and the HTL/perovskite interfaces. This can be seen from Figure 4b: when carriers are generated closer to the ETL interface (longer wavelengths), EQE almost doubles, while carriers generated closer to the HTL interface only lead to slight EQE enhancements. This effect can be seen even more clearly by comparing the photocurrent map at 720 nm (Figure 2b)—which shows dramatic spatial variations—to that at 410 nm (Figure S4, Supporting Information), which is homogeneous. At short wavelengths where absorption happens near the surface, surface recombination dominates, while at longer wavelengths the difference in recombination rates at the ETL and HTL interfaces become relevant.

Carrier extraction is the third major loss mechanism. This is clear from the very high device PLQY—approaching that of record GaAs solar cells—combined with the low V_{OC} , J_{SC} , and FF values. If nonradiative recombination at the contacts, surface or in the perovskite were the main loss mechanism limiting efficiency, it would not be possible to measure such high PLQY values. The absorption measurements also confirm that enough light is collected to reach much higher efficiencies. Measurements of leakage current through the dielectric showed nothing above the noise floor (approximately 5 pA, as shown in Figure S7 in the Supporting Information). Altogether this suggests that the primary problem is a very large extraction barrier at either the ETL, HTL, or both. Given that the SnO_2 has been used extensively for high efficiency perovskite solar cells, we postulate that this barrier is primarily caused by the HTL. The substantial light bias dependence of the EQE (Figure S6, Supporting Information) is consistent with an extraction barrier caused by poor Fermi level alignment or insufficient HTL doping. In addition, an s-shaped JV curve is observed when scanning the sample over a larger voltage range (Figure S8, Supporting Information). This further confirms the carrier extraction barrier.

Given the three loss mechanisms described above we can suggest three concrete steps to improve performance in back-contact perovskite solar cells. First, a top surface passivation layer is re-

quired to improve the blue response of the cells. The reduced surface recombination will also boost the V_{OC} .^[41] If chosen correctly, this layer can serve a dual function as an antireflection (AR) coating and encapsulation layer. Silicon oxide and aluminum oxide have been shown to provide excellent passivation and improved stability, but SiO_2 is likely preferable due to its nearly ideal refractive index for an AR coating. Second, the NiO_x HTL needs to be replaced or modified to reduce the interfacial recombination rate and especially lower the extraction barrier. Currently thermal oxidation is used to form the NiO_x HTL, but electrodeposition might be a more suitable technique since it can provide much more flexibility in the HTL material choice, including the use of dopants to tune the Fermi level and carrier density.

5. Conclusion

In this paper, we have fabricated grid-shaped back-contact perovskite solar cells with SnO_2 as ETL and NiO_x as HTL and measured their electrical and optical properties with micron-scale spatial resolution. The combination of absorption, photocurrent, photovoltage, EQE, PLQY, and PL lifetime mapping provides a powerful suite of characterization tools to gain insights into the loss mechanisms and develop a path forward for improved device efficiency. Our results suggest the ultimate efficiency of back-contact perovskite devices can approach record efficiency GaAs solar cells since the PLQY of the devices, which is an indication of the maximum achievable V_{OC} , is already approaching the highest value ever recorded for operating solar cells. Moving forward the biggest improvement will come from replacing or modifying the NiO_x HTL, which currently shows a large extraction barrier and substantial interface recombination. Higher efficiency, particularly from improved blue response, can also be reached by passivating the surface with a transparent dielectric that can serve a triple function as AR coating and encapsulation layer for improved stability. These results suggest the back-contact perovskite solar cell geometry is promising for reaching the ultimate device efficiency and deserves further study.

Supporting Information

Supporting Information is available from the Wiley Online Library or from the author.

Acknowledgements

E.C.G. proposed the project. S.G. performed the lifetime measurement. S.A.R. and J.S.B. performed the PLQY and absorption measurement. H.S. fabricated the devices and did the rest of the measurements. K.D. helped with perovskite synthesis. H.S., S.G., and E.C.G. wrote the manuscript. This work was supported by the Netherlands Organization for Scientific Research (NWO) through the Joint Solar Program III.

Conflict of Interest

The authors declare no conflict of interest.

Data Availability Statement

The data that support the findings of this study are available from the corresponding author upon reasonable request.

Keywords

back-contact solar cells, current mapping, loss processes, perovskites

Received: February 16, 2023
Revised: April 30, 2023
Published online:

- [1] K. Yoshikawa, W. Yoshida, T. Irie, H. Kawasaki, K. Konishi, H. Ishibashi, T. Asatani, D. Adachi, M. Kanematsu, H. Uzu, K. Yamamoto, *Sol. Energy Mater. Sol. Cells* **2017**, *173*, 37.
- [2] NREL. Best Research Cell Efficiency Chart. <https://www.nrel.gov/pv/moduleefficiency.html> (accessed: October 2022).
- [3] A. Richter, M. Hermle, S. Glunz, *IEEE J. Photovoltaics* **2013**, *07*, 1184.
- [4] K. Masuko, M. Shigematsu, T. Hashiguchi, D. Fujishima, M. Kai, N. Yoshimura, T. Yamaguchi, Y. Ichihashi, T. Mishima, N. Matsubara, T. Yamanishi, T. Takahama, M. Taguchi, E. Maruyama, S. Okamoto, *IEEE J. Photovoltaics* **2014**, *4*, 1433.
- [5] K. Yoshikawa, H. Kawasaki, W. Yoshida, T. Irie, K. Konishi, K. Nakano, T. Uto, D. Adachi, M. Kanematsu, H. Uzu, K. Yamamoto, *Nat. Energy* **2017**, *2*, 17032.
- [6] A. Fell, J. Greulich, F. Feldmann, C. Messmer, J. Schön, M. Bivour, M. Schubert, S. Glunz, *Sol. Energy Mater. Sol. Cells* **2022**, *236*, 111534.
- [7] C. Messmer, A. Fell, F. Feldmann, N. Wöhrle, J. Schön, M. Hermle, *IEEE J. Photovoltaics* **2019**, *10*, 335.
- [8] X. Mackrè-Delannoy, G. Hamon, M. Volatier, A. Jaouad, V. Aimez, M. Darnon, *AIP Conf. Proc.* **2020**, *2298*, 020005.
- [9] R. Gottschalg, B. Elsworth, D. Infield, K. M. In, *Investigation of the Back Contact of CdTe Solar Cells*, 1999 ISES Solar World Congress, Elsevier Science, **2000**, p. 124, <https://shop.elsevier.com/books/1999-ises-solar-world-congress/grossman/978-0-08-043895-5>.
- [10] N. Romeo, A. Bosio, S. Mazzamuto, D. Menossi, J. L. Peña, A. Salavei, I. Rimmaudo, V. Allodi, A. Romeo, in 26th EU PVSEC **2011**, pp. 2460–2462, <https://doi.org/10.4229/26thEUPVSEC2011-3DO.9.4>.
- [11] R. S. Hall, D. Lamb, S. J. C. Irvine, *Energy Sci. Eng.* **2021**, *9*, 606.
- [12] M. Nardone, M. Spehar, D. Kuciauskas, D. Albin, *J. Appl. Phys.* **2020**, *127*, 223104.
- [13] D. Josell, R. Debnath, J. Y. Ha, J. Guyer, M. A. Sahiner, C. J. Reehil, W. A. Manners, N. V. Nguyen, *ACS Appl. Mater. Interfaces* **2014**, *6*, 15972.
- [14] A. N. Jumabekov, E. Della Gaspera, Z. Q. Xu, A. S. R. Chesman, J. van Embden, S. A. Bonke, Q. Bao, D. Vak, U. Bach, *J. Mater. Chem. C* **2016**, *4*, 3125.
- [15] G. D. Tainter, M. T. Hörantner, L. M. Pazos-Outón, R. D. Lamboll, H. Abolinš, T. Leijtens, S. Mahesh, R. H. Friend, H. J. Snaith, H. J. Joyce, F. Deschler, *Joule* **2019**, *3*, 1301.
- [16] Q. Hou, D. Bacal, A. N. Jumabekov, W. Li, Z. Wang, X. Lin, S. H. Ng, B. Tan, Q. Bao, A. S. R. Chesman, Y. Cheng, U. Bach, *Nano Energy* **2018**, *50*, 710.
- [17] M. Wong-Stringer, T. J. Routledge, T. McArdle, C. J. Wood, O. S. Game, J. A. Smith, J. E. Bishop, N. Vaenas, D. M. Coles, A. R. Buckley, D. G. Lidzey, *Energy Environ. Sci.* **2019**, *12*, 1928.
- [18] K. J. Prince, C. P. Muzzillo, M. Mirzokarimov, C. A. Wolden, L. M. Wheeler, *ACS Appl. Energy Mater.* **2022**, *5*, 9273.
- [19] K. J. Prince, M. Nardone, S. P. Dunfield, G. Teeter, M. Mirzokarimov, E. L. Warren, D. T. Moore, J. J. Berry, C. A. Wolden, L. M. Wheeler, *Cell Rep. Phys. Sci.* **2021**, *2*, 100363.
- [20] T. Fuyuki, H. Kondo, T. Yamazaki, Y. Takahashi, Y. Uraoka, *Appl. Phys. Lett.* **2005**, *86*, 262108.
- [21] P. Würfel, T. Trupke, T. Puzzer, E. Schäffer, W. Warta, S. W. Glunz, *J. Appl. Phys.* **2007**, *101*, 123110.
- [22] G. W. P. Adhyaksa, L. W. Veldhuizen, Y. Kuang, S. Brittan, R. E. I. Schropp, E. C. Garnett, *Chem. Mater.* **2016**, *28*, 5259.
- [23] S. D. Stranks, G. E. Eperon, G. Grancini, C. Menelaou, M. J. P. Alcocer, T. Leijtens, L. M. Herz, A. Petrozza, H. J. Snaith, *Science* **2013**, *342*, 341.
- [24] E. Edri, S. Kirmayer, S. Mukhopadhyay, K. Gartsman, G. Hodes, D. Cahen, *Nat. Commun.* **2014**, *5*, 3461.
- [25] O. E. Semonin, G. A. Elbaz, D. B. Straus, T. D. Hull, D. W. Paley, A. M. van der Zande, J. C. Hone, I. Kymissis, C. R. Kagan, X. Roy, J. S. Owen, *J. Phys. Chem. Lett.* **2016**, *7*, 3510.
- [26] G. W. Adhyaksa, E. Johlin, E. C. Garnett, *Nano Lett.* **2017**, *17*, 5206.
- [27] S. A. Mann, B. Sciacca, Y. Zhang, J. Wang, E. Kontoleta, H. Liu, E. C. Garnett, *ACS Nano* **2017**, *11*, 1412.
- [28] S. A. Mann, S. Z. Oener, A. Cavalli, J. E. M. Haverkort, E. Bakkers, E. C. Garnett, *Nat. Nanotechnol.* **2016**, *11*, 1071.
- [29] D. M. Bacal, N. N. Lal, A. N. Jumabekov, Q. Hou, Y. Hu, J. Lu, A. S. R. Chesman, U. Bach, *Opt. Express* **2020**, *28*, 12650.
- [30] X. Lin, J. Lu, S. R. Raga, D. P. McMeekin, Q. Ou, A. D. Scully, B. Tan, A. S. R. Chesman, S. Deng, B. Zhao, Y. B. Cheng, U. Bach, *Adv. Energy Mater.* **2021**, *11*, 2100053.
- [31] J. J. Yoo, G. Seo, M. R. Chua, T. G. Park, Y. Lu, F. Rotermund, Y. Kim, C. S. Moon, N. J. Jeon, J. P. Correa-Baena, V. Bulvić, S. S. Shin, M. G. Bawendi, J. Seo, *Nature* **2021**, *590*, 587.
- [32] J. Zhang, C. Bai, Y. Dong, W. Shen, Q. Zhang, F. Huang, Y. Cheng, J. Zhong, *Chem. Eng. J.* **2021**, *425*, 131444.
- [33] M. Saliba, T. Matsui, J. Y. Seo, K. Domanski, J. P. Correa-Baena, M. K. Nazeeruddin, S. M. Zakeeruddin, W. Tress, A. Abate, A. Hagfeldt, M. Grätzel, *Energy Environ. Sci.* **2016**, *9*, 1989.
- [34] H. B. Lee, N. Kumar, M. M. Ovhal, Y. J. Kim, Y. M. Song, J. W. Kang, *Adv. Funct. Mater.* **2020**, *30*, 2001559.
- [35] L. Hirvonen, K. Suhling, *Front. Phys.* **2020**, *5*, 8.

- [36] M. Green, *Prog. Photovoltaics Res. Appl.* **2012**, 6, 20.
- [37] S. A. Mann, S. Z. Oener, A. Cavalli, J. E. Haverkort, E. P. Bakkers, E. C. Garnett, *Nat. Nanotechnol.* **2016**, 11, 1071.
- [38] U. Rau, *Phys. Rev. B* **2007**, 76, 085303
- [39] J. Warby, F. Zu, S. Zeiske, E. Gutierrez-Partida, L. Frohloff, S. Kahmann, K. Frohna, E. Mosconi, E. Radicchi, F. Lang, S. Shah, F. Peña-Camargo, H. Hempel, T. Unold, N. Koch, A. Armin, F. D. Angelis, S. D. Stranks, D. Neher, M. Stolterfoht, *Adv. Energy Mater.* **2022**, 12, 2103567.
- [40] M. Abdi-Jalebi, Z. Andaji-Garmaroudi, S. Cacovich, C. Stavrides, B. Philippe, J. M. Richter, M. Alsari, E. P. Booker, E. M. Hutter, A. J. Pearson, S. Lilliu, T. J. Savenije, H. Rensmo, G. Divitini, C. Ducati, R. H. Friend, S. D. Stranks, *Nature* **2018**, 555, 497
- [41] S. Jariwala, S. Burke, S. Dunfield, R. C. Shallcross, M. Taddei, J. Wang, G. E. Eperon, N. R. Armstrong, J. J. Berry, D. S. Ginger, *Chem. Mater.* **2021**, 33, 5035
- [42] L. Krückemeier, B. Krogmeier, Z. Liu, U. Rau, T. Kirchartz, *Adv. Energy Mater.* **2021**, 11, 2003489.